

# Synchrotron Radiation Masking in the PEP-II High-Energy Ring\*

M. Nordby, J. Hodgson

Stanford Linear Accelerator Center, Stanford University, Stanford, CA 94309

M. Fong

Lawrence Berkeley Laboratory, Berkeley, CA 94720

## Abstract

The high current, large bending radius, and high photon flux of the PEP-II high-energy ring dictate the use of both distributed and discrete synchrotron radiation (SR) absorbers. This combined masking design is presented, and thermal and structural analyses are discussed. Analysis results show how the Oxygen-Free Electronic (OFE) copper chamber will reliably absorb the distributed radiation load, while high-strength Glidcop successfully withstands the higher thermal stresses of the discrete masks. Implications for fabrication are discussed.

## ARC CELL LAYOUT

The PEP-II High-Energy Ring (HER) electron storage ring is a 2 km long hexagon, with the corners rounded into 224 m long arc sections. An arc consists of 32 half-cells, each of which contain a 5 m long bending magnet, with a 165 m bending radius, followed by a 2 m long straight section containing a pumping chamber and a sextupole, quadrupole, and corrector magnet. See Figure 1.

As the electron beam bends through the 5 m long dipole bend field, it emits synchrotron radiation (SR). This radiation fans out tangentially from the beam arc and intercepts the outer wall of the vacuum chamber, both in the dipole chamber and in the short, straight quad chamber.

## DISTRIBUTED POWER ABSORPTION IN CHAMBERS

Such a high-power, distributed SR fan suggests the use of a continuous absorber to intercept the radiation at the vacuum chamber wall. This absorber is actually part of the wall of the beam chamber itself. Figure 2 shows the chamber cross sections, which are as large as possible to maximize conductance, yet small enough to fit through all magnet pole tips. All cooling for the absorber/wall is outside the vacuum, so no complicated end connections are needed. Both chambers are extruded from Oxygen-Free Electronic (OFE) grade copper to exploit its high conductivity and low gas desorption rate.

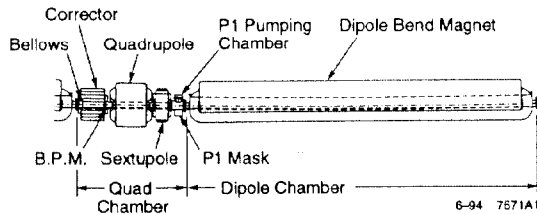


Figure 1. Plan view of arc half-cell.

\*Work supported by Department of Energy contract DE-AC03-76SF00515 (SLAC) and DE-AC03-76SF0098 (LBL).

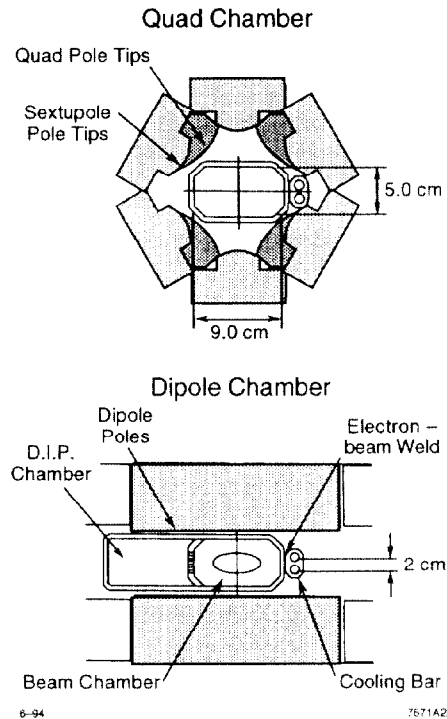


Figure 2. Dipole and quad chamber cross sections.

## Thermal Analysis of the Cross Section

The 9 GeV, 3000 mA electron beam emits a fan of high-density SR that strikes the chamber wall at a peak density of  $2320 \text{ W/cm}^2$ , on a strip 0.044 cm high, vertically centered and running the length of the chamber. This integrates to 55 kW for a half-cell. The loading is applied every time the beam is cycled, so the alternating stress produced in the chamber must not exceed 26,000 psi, which is the 10,000-cycle fatigue strength for OFE copper. The chamber is water cooled, with a film coefficient of  $1.0 \text{ W/cm}^2 \cdot ^\circ\text{C}$  at a mass flow rate of 0.13 kg/sec per hole. The double-holed cooling bar provides better heat transfer to the water than a single slot, while still providing a good electron-beam weld joint and a shape which can be extruded.

A thermal finite-element analysis of the cross-section of the dipole chamber, using ANSYS from Swanson Analysis Systems, Inc., produces the temperature profile shown in Figure 3. The peak temperature of  $103^\circ\text{C}$  occurs at the center of the heated region, while most of the vacuum chamber reaches a uniform bulk temperature of  $63^\circ\text{C}$ .

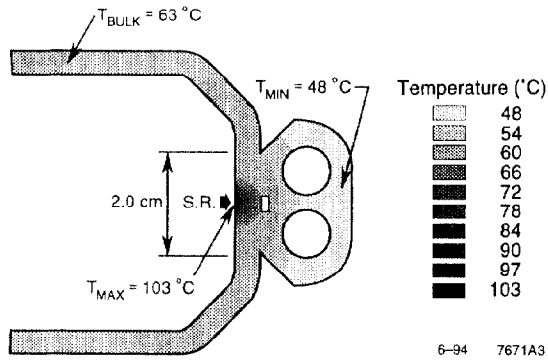


Figure 3. Temperature profile in a dipole chamber cross-section.

### Structural Analysis of the Cross Section

The temperature profile calculated above serves as the input to a structural analysis of the cross section. A 0.05 cm thick slice of the chamber was modeled and constrained such that the stresses and strains computed are identical to those that would exist far from the ends of a long chamber.

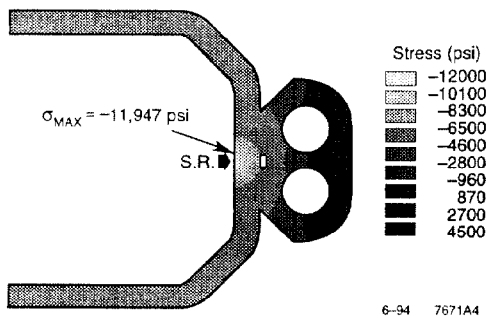


Figure 4. Axial stress in a dipole chamber cross-section.

A plot of the resultant z- or axial-stress is shown in Figure 4. The peak stress in the chamber is an 11,947 psi compressive stress, occurring in the SR impingement zone. This results from the difference between the peak temperature and the bulk temperature of the chamber. Indeed, the simple equation

$$\begin{aligned} \sigma_{\text{axial}} &= E\alpha (T_{\text{bulk}} - T_{\text{max}}) \\ &= (17 \times 10^6 \text{ psi}) (17 \times 10^{-6} / ^\circ\text{C}) \\ &\quad \times (63^\circ\text{C} - 103^\circ\text{C}) \\ &= -11,560 \text{ psi} \end{aligned}$$

indicates that the high compressive stress is due almost entirely to the small hot spot being restrained from expanding any more than the bulk of the chamber expands.

Thus, to minimize the peak stress, the structural analysis shows that it is most important to reduce the difference between the peak and bulk temperatures, and not their independent values. Preliminary analysis of various electron-beam weld joints showed that the nominal chamber temperature can be reduced by increasing the weld length or moving the cooling channels, but this would increase the temperature

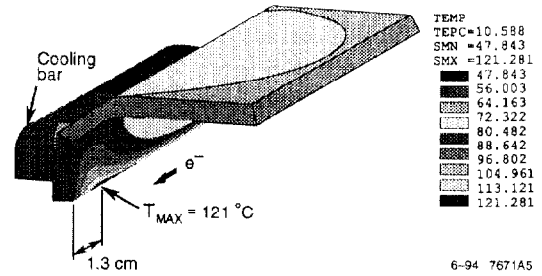


Figure 5. Temperature distribution at end of dipole chamber.

difference and, thus, the peak stress. The present design strikes a compromise between the conflicting demands of decreasing the temperature differential, yet maintaining reasonable temperatures in the chamber.

### End effects

The temperature profile changes near the chamber ends because the cooling bar stops 3.4 cm before the end of the chamber, while the SR continues to 1.3 cm, where a back-slant starts to cast a shadow over the flange joint. The maximum temperature of 121°C occurs at the start of this back-slant, where the SR ends and the shadow begins. At this point, the cooling has ended, so the heat must conduct back upstream to reach the cooling bar. Figure 5 shows the temperature distribution of the final 10 cm of the chamber.

Not surprisingly, the higher temperature at the end produces a higher axial stress. The peak compressive axial stress is -13,700 psi, and occurs at the peak temperature location (see Figure 6). Note that the axial stress distribution looks similar to the temperature distribution, and is 15% higher than the mid-chamber stress. As expected, it quickly dies down from its peak to zero at the end of the chamber, and to the nominal compressive stress of -12,000 psi moving into the chamber.

### Fabrication Implications

To withstand the high operational stresses, half-hard OFE copper will be used for the chambers. This temper is attained by extruding and drawing the entire chamber as a single piece.

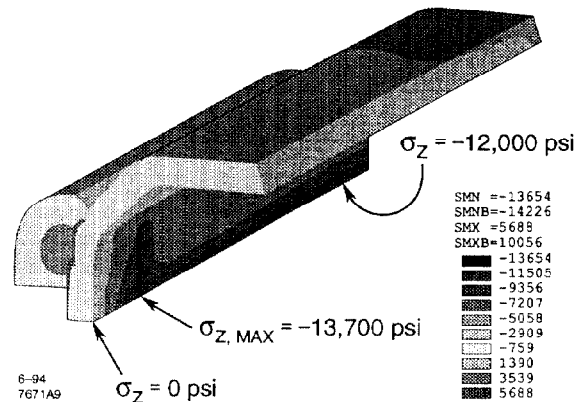


Figure 6. Axial stress distribution at end of dipole chamber.

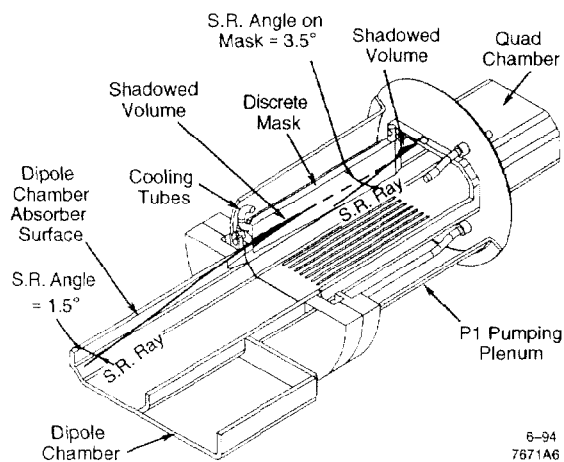


Figure 7. Discrete mask inside pumping and dipole chambers.

The cooling bar is then joined to the chamber using electron-beam welding. Our tests have shown that, after the cooling bar is joined to the chamber, the SR impingement zone remains half-hard, despite its proximity to the weld. Following the welding of the cooling bar, the dipole chamber is bent by simultaneously stretching and bending the chamber, which minimizes added residual stress.

### DISCRETE MASKING

The discrete mask provides shadowing for uncooled components that otherwise could not withstand the power of the direct SR. Figure 7 shows the mask inside its pumping plenum, where it is mounted in a slot cut in the wall of the quadrupole chamber.

The mask is made from Glidcop dispersion-strengthened copper. Glidcop combines the high thermal conductivity of OFE copper, with a very high yield and fatigue strength, even when annealed.

#### Thermal Analysis of the mask

The 2° slope of the mask produces a synchrotron radiation power density of 4476 W/cm<sup>2</sup> on a band 0.049 cm high. Stainless steel tubes provide water cooling at 0.09 kg/sec, with a convection coefficient of 1.85 W/cm<sup>2</sup>·°C. Finite-element heat transfer analysis (using I-DEAS from Structural Dynamics Research, Corp.) produces the temperature contour plot shown in Figure 8. The peak temperature of 211°C shows the impact of nearly doubling the incoming SR power. The spread between the peak and minimum temperature has also increased from 55°C for the chamber to 145°C for the mask. Part of this increase results from the higher power flux, but some is attributed to the higher temperature gradient across the poorly-conducting stainless steel cooling tubes.

#### Structural Analysis of the Mask

Structural analysis shows that the peak stress in the mask is also higher than in the chamber. The axial stress at the SR impingement zone of the mask reaches -33,000 psi,

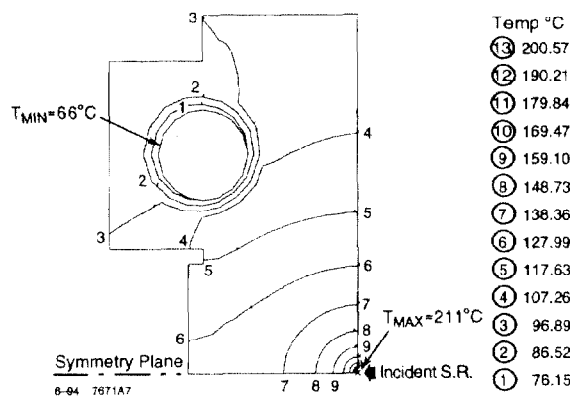


Figure 8. Temperature plot of the mask cross section.

compared with only -11,950 psi for the chamber cross-section. The higher temperature differential clearly accounts for much of this additional stress. The cross-sectional stress contour plot of Figure 9 shows how the peak compressive stress in the Glidcop mask body and the high tensile stress in the relatively cold stainless steel tubing balance each other. For Glidcop, the fatigue strength for 10,000-cycle loading exceeds 60,000 psi, so the -33,000 psi design stress will not produce fatigue failure.

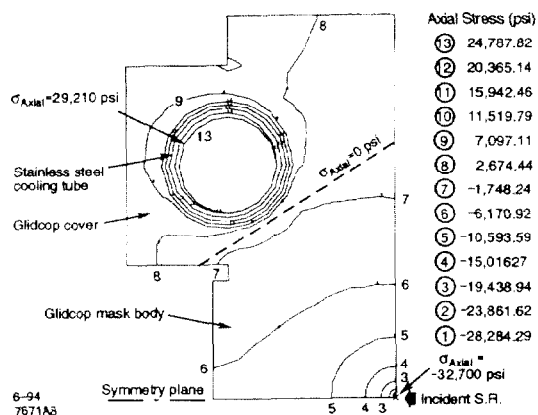


Figure 9. Axial Stress in Mask Cross-section

Finally, at the ends of the mask, the SR stops as the mask enters a shadow on the upstream end, and is back-cut on the downstream end. Thus, unlike the continuous absorber of the dipole chamber, the ends of the mask do not have uncooled regions, and therefore the high axial stress dies down to zero as the SR stops.

### CONCLUSION

Thermal and structural analysis of both the continuous and discrete absorber show that they can endure the high heat flux produced by the synchrotron radiation. Stresses in the elastic regime are below the materials' 10,000-cycle fatigue strengths to ensure conservative operational loading. Fabrication processes have been developed that preserve the strength of the materials and minimize residual stresses to maintain this margin of security.